

Geometric Electrostatic Particle-In-Cell Algorithm on Unstructured Meshes

Zhenyu Wang, Hong Qin, Benjamin Sturdevant, Choong-Seock Chang¹

¹*Princeton Plasma Physics Laboratory,
Princeton University, Princeton, NJ 08543*

arXiv:2012.08587v2 [physics.plasm-ph] 17 Dec 2020

Abstract

We present a geometric Particle-in-Cell (PIC) algorithm on two-dimensional (2D) unstructured meshes for studying electrostatic perturbations in magnetized plasmas. In this method, ions are treated as fully kinetic particles, and electrons are described by the adiabatic response. The PIC method is derived from a discrete variational principle on unstructured meshes. To preserve the geometric structure of the system, the discrete variational principle requires that the electric field is interpolated using Whitney 1-forms, the charge is deposited using Whitney 0-forms, and the electric field is computed by discrete exterior calculus. The algorithm has been applied to study the Ion Bernstein Wave (IBW) in 2D magnetized plasmas. The simulated dispersion relations of the IBW in a rectangular region agree well with theoretical results. In a 2D circular region with the fixed boundary condition, the spectrum and eigenmode structures of the IBW are determined from simulation. We compare the energy conservation property of the geometric PIC algorithm derived from the discrete variational principle with that of previous PIC methods on unstructured meshes. The comparison shows that the new PIC algorithm significantly improves the energy conservation property.

I. INTRODUCTION

Particle-In-Cell (PIC) simulation is an important tool for plasma physics [1–5]. Structured mesh is easy to implement and widely used in PIC simulations. On the other hand, some studies require modeling plasma behaviors in specific and complex geometries, where unstructured meshes have a unique advantage. Electrostatic (ES) PIC schemes on unstructured meshes have been proposed [6–10]. In these schemes, the shape function for interpolating the electric field at particles' positions is identical to that for depositing particles' charge to the grid points of unstructured meshes. Numerical studies [11] showed that using the same shape function for charge deposition and field interpolation restricts the grid size to the Debye length. It is difficult to carry out large-scale simulations for collisionless plasma using these ES PIC schemes. In previous PIC methods, the charge-deposition algorithm and the field-interpolation algorithm are independent. The shape functions for these two algorithms can be chosen to be the same or different. There is no fundamental guiding principle on how to design these two algorithms. In the present study, we develop a geometric

algorithm for ES PIC simulations with adiabatic electrons on an unstructured mesh. Instead of select a shape function based on intuition or experience, we derive the charge-deposition and field-interpolation algorithm from an underpinning discrete variational principle.

Squire et al. [12, 13] first employed the methodology of discrete variational principle [14–19] to derive an electromagnetic (EM) PIC algorithm on an unstructured mesh. In this work, the technique of Whitney forms [20] were introduced for the first time to deposit charge and current and to interpolate fields. Discrete Exterior Calculus (DEC) [21, 22] was also applied to compute the electromagnetic field on the unstructured mesh. It was demonstrated that the discrete variational principle admits the discrete electromagnetic gauge symmetry and thus ensures the discrete charge conservation [12, 13, 23–25]. Xiao et al. [23] developed an explicit high-order non-canonical symplectic electromagnetic PIC schemes starting from the discrete variational principles on a cubic mesh. High-order Whitney forms for cubic meshes were constructed and used for the current deposition and electromagnetic field interpolation. It was found that the “shape functions” for current deposition and field interpolation are different, and even for different components of the field the interpolation schemes are different. Similar and subsequent studies [26–31] have also illustrated that discrete variational principles and Whitney forms are useful tools in designing structure-preserving geometric PIC algorithms [12, 13, 23, 24, 32–40]. Even for partially-geometric PIC algorithms, the application of Whitney forms has been found to be beneficial [41].

In plasma physics, many reduced models are used. It is desirable to apply structure-preserving geometric algorithms to these models as well. One widely adopted reduced model is the Vlasov-Poisson system with kinetic ions and adiabatic electrons. A structure-preserving geometric PIC algorithm on a cubic mesh for this system was developed recently [29]. The construction of the algorithm starts from a field theory, i.e., a variational principle. As in the geometric PIC algorithms for the Vlasov-Maxwell system, Whitney forms and variational symplectic integrators are employed. In particular, the charge-deposition and field-interpolation schemes were derived from the variational principle for the electrostatic dynamics in the cubic mesh.

We take a step-by-step approach to extend the structure-preserving geometric PIC algorithm for the Vlasov-Poisson system reported in Ref. [29] to unstructured meshes. In the present work, we focus on the charge-deposition and field-interpolation methods and have not implemented the symplectic integrator. The Lagrangian of the system is discretized on

an unstructured mesh, and the charge-deposition and field-interpolation methods are derived from the discrete variational principle on the unstructured mesh using Whitney forms. In place of a more structure-preserving symplectic integrator [32, 34, 42], the Boris algorithm [43], which preserves the phase space volume [44–48], is adopted to push particles. Our purpose here is to demonstrate how to design effective charge-deposition and field-interpolation algorithms on an unstructured mesh using the discrete field theory and Whitney forms. To validate the new PIC algorithm, we compare the dispersion relation of the Ion Bernstein Wave (IBW) from the PIC simulation with the theory [49, 50] in a two-dimensional (2D) periodic plasma. Eigenmode structures of the IBW in a 2D circular geometry with Dirichlet boundary conditions are also simulated. We compare the simulation results with those of the conventional methods [6, 7] on the same unstructured mesh, and find that our method is able to significantly reduce the energy error of the simulations.

The paper is organized as follows. In Sec. II, the geometric electrostatic PIC algorithm with fully kinetic ions and adiabatic electrons on an unstructured mesh is derived. Simulations of the IBW in an infinite 2D geometry and a 2D circular geometry are presented in Sec. III. We compare the energy conservation property of our algorithm with that of previous methods in Sec. IV.

II. GEOMETRIC ELECTROSTATIC PIC ALGORITHM ON AN UNSTRUCTURED MESH

In this section, we extend the geometric electrostatic PIC algorithm reported in Ref. [29] to an unstructured mesh. The model treats ions as fully kinetic 6D particles. The response of the electrons is adiabatic [49, 51–54], which, with the quasi-neutrality condition, leads to

$$-\frac{q_i}{q_e}n_i = n_{e0}\exp\left(-\frac{q_e\phi}{T_e}\right), \quad (1)$$

where n_i is the ion density, n_{e0} the background electron density, ϕ the electric potential, T_e the electron temperature, and q_e and q_i are electron and ion charges respectively. The

action integral of the system is [29]

$$S(\mathbf{x}, \phi) = \int dt L(\mathbf{x}, \phi), \quad (2)$$

$$L = \int d\mathbf{x} d\mathbf{v} f_i(\mathbf{x}, \mathbf{v}) \left[\frac{1}{2} m_i \dot{\mathbf{x}}^2 + q_i \dot{\mathbf{x}} \cdot \mathbf{A}_0(\mathbf{x}, t) \right] - q_i [\phi(\mathbf{x}, t) + \phi_0(\mathbf{x}, t)] + n_{e0} T_e \exp \left[-\frac{q_e \phi(\mathbf{x}, t)}{T_e} \right], \quad (3)$$

where $\mathbf{x} = \mathbf{x}(\mathbf{x}_0, \mathbf{v}_0, t)$, f_i is the ion distribution function, m_i is ion mass, and \mathbf{A}_0 and ϕ_0 are the external vector and scalar potentials. The dynamics of the system is governed by the Euler-Lagrange equations,

$$\frac{\delta S}{\delta \phi} = 0, \quad (4)$$

$$\frac{\delta S}{\delta \mathbf{x}} = 0. \quad (5)$$

Equation (4) links the electric potential ϕ and the ion charge density ρ_i ,

$$\phi = -\frac{T_e}{q_e} \log \left(-\frac{\rho_i}{q_e n_{e0}} \right), \quad (6)$$

where $\rho_i = \int d\mathbf{v} q_i f_i(\mathbf{x}, \mathbf{v})$. Equation (6) recovers the electron adiabatic response and charge-neutrality condition in Eq. (1). Equation (5) gives equation of motion for particles,

$$\ddot{\mathbf{x}} = \frac{q_i}{m_i} [\mathbf{E}_0(\mathbf{x}, t) + \mathbf{E}(\mathbf{x}, t) + \dot{\mathbf{x}} \times \mathbf{B}_0(\mathbf{x}, t)], \quad (7)$$

where $\mathbf{E}_0(\mathbf{x}, t)$ and $\mathbf{B}_0(\mathbf{x}, t)$ are the external electromagnetic field, and $\mathbf{E}(\mathbf{x}, t) = -\nabla \phi(\mathbf{x}, t)$ is the perturbed electrostatic field.

We use the method introduced in Refs. [12, 29] to discretize the action integral by particles and Whitney forms [20] on a 2D unstructured triangular mesh. The discrete action integral S_d can be written as

$$S_d(\mathbf{x}_p, \phi_I) = \int L_d(\mathbf{x}_p, \phi_I) dt, \quad (8)$$

$$L_d(\mathbf{x}_p, \phi_I) = \sum_p \left[\frac{1}{2} m_i \dot{\mathbf{x}}_p^2 + q_i \dot{\mathbf{x}}_p \cdot \mathbf{A}_0(\mathbf{x}_p) - q_i \sum_I W_{\sigma_0, I}(\mathbf{x}_p) \phi_I - q_i \phi_0(\mathbf{x}_p) \right] + \sum_I n_{e0, I} T_{e, I} \exp \left(-\frac{q_e \phi_I}{T_{eI}} \right), \quad (9)$$

where I is triangular vertex index, \mathbf{x}_p the particle position of the p -th particle, ϕ_I is the electric potential defined on the triangular vertex, and $W_{\sigma_0, I}$ is the Whitney 0-form interpolating the value of ϕ in the continuous space using ϕ_I . The discrete action integral is the same as in Ref. [29], except that here it is on a 2D unstructured triangular mesh.

Variations of S_d with respect to ϕ_I and \mathbf{x}_p lead to the equations of motion of the electrostatic system,

$$\frac{\delta S}{\delta \phi_I} = 0, \quad (10)$$

$$\frac{\delta S}{\delta \mathbf{x}_p} = 0. \quad (11)$$

Equation (10) gives

$$\phi_I = -\frac{T_{e,I}}{q_e} \log\left(-\frac{\rho_I}{q_e n_{e0,I}}\right), \quad (12)$$

where

$$\rho_I = q_i W_{\sigma_0,I}(\mathbf{x}_p) \quad (13)$$

is the charge density on the triangular vertex. Equation (11) is the governing equation for ion dynamics,

$$\ddot{\mathbf{x}}_p = \frac{q_i}{m_i} \left[\mathbf{E}_0(\mathbf{x}_p, t) + \dot{\mathbf{x}}_p \times \mathbf{B}_0(\mathbf{x}_p, t) - \frac{\partial}{\partial \mathbf{x}_p} \sum_I W_{\sigma_0,I}(\mathbf{x}_p) \phi_I \right]. \quad (14)$$

The last term of Eq. (14) is the derivative of $W_{\sigma_0,I}$ with respect to \mathbf{x}_p in the continuous space. According to the property of Whitney forms [12, 20, 22, 23],

$$\nabla \sum_I W_{\sigma_0,I}(\mathbf{x}_p) \phi_I = \sum_J W_{\sigma_1,J}(\mathbf{x}_p) \sum_I \nabla_{dJ,I} \phi_I. \quad (15)$$

where $\sum_I \nabla_{dJ,I} \phi_I$ is the discrete gradient of ϕ_I , and $W_{\sigma_1,J}$ is the Whitney 1-form that interpolates a continuous 1-form from the discrete 1-form defined on the triangular edge. The construction of $W_{\sigma_0,I}$, $W_{\sigma_1,J}$ and $\nabla_{dJ,I}$ will be discussed shortly after. With property (15), Eq. (14) becomes

$$\ddot{\mathbf{x}}_p = \frac{q_i}{m_i} \left[\mathbf{E}_0(\mathbf{x}_p, t) + \dot{\mathbf{x}}_p \times \mathbf{B}_0(\mathbf{x}_p, t) + \sum_J W_{\sigma_1,J}(\mathbf{x}_p) \mathbf{E}_J \right], \quad (16)$$

and

$$\mathbf{E}_J = -\sum_I \nabla_{dJ,I} \phi_I, \quad (17)$$

where \mathbf{E}_J is the discrete electrical field defined on the triangular edge labeled by J . We want to emphasize again that, similar to the scenario in a cubic mesh [29], without Whitney forms and DEC, it is difficult to calculate on the electric field on an unstructured mesh to advance particles' positions.

As is well-known, the key parts of a PIC method include charge deposition, solving discrete field, and field interpolation, which are encapsulated in a systematic way in Eqs. (13),

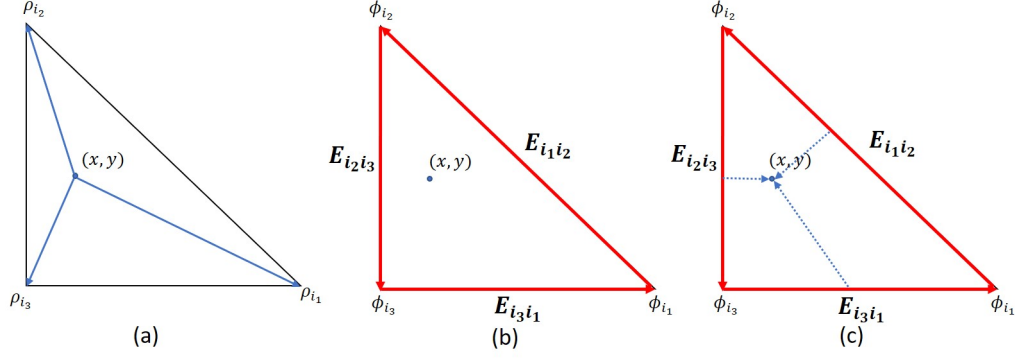


Figure 1. The PIC algorithm on a triangle. (a) Depositing a particle's charge to the triangular vertices using Whitney 0-forms $W_{\sigma_0, I}$. (b) Computing \mathbf{E}_J on the edge with the discrete gradient operator $\nabla_{dJ, I}$. (c) Interpolating \mathbf{E}_J from edges to the particle's location through Whitney 1-forms $W_{\sigma_1, J}$.

(17), and (16), respectively. Once $W_{\sigma_0, I}$, $W_{\sigma_1, J}$ and $\nabla_{dJ, I}$ are chosen, the PIC algorithm is defined.

Now we describe in details the construction of $W_{\sigma_0, I}$, $W_{\sigma_1, J}$ and $\nabla_{dJ, I}$ on the triangular mesh. Figure 1(a) shows a particle in a triangle, (x, y) is the position of the particle p , and the three vertices of the i -th triangle, i_1, i_2, i_3 , have coordinates $(x_{i_1}, y_{i_1}), (x_{i_2}, y_{i_2}), (x_{i_3}, y_{i_3})$, respectively. To deposit charge at each vertex according to Eq. (13), we need to specify the Whitney 0-forms, which are chosen to be linear barycentric functions. For (x, y) inside the triangle, the Whitney 0-forms are

$$W_{\sigma_0, i_1}(x, y) = \frac{(y_{i_2} - y_{i_3})(x - x_{i_3}) + (x_{i_3} - x_{i_2})(y - y_{i_3})}{(x_{i_1} - x_{i_3})(y_{i_2} - y_{i_3}) + (x_{i_3} - x_{i_2})(y_{i_1} - y_{i_3})}, \quad (18)$$

$$W_{\sigma_0, i_2}(x, y) = \frac{(y_{i_3} - y_{i_1})(x - x_{i_3}) + (x_{i_1} - x_{i_3})(y - y_{i_3})}{(x_{i_1} - x_{i_3})(y_{i_2} - y_{i_3}) + (x_{i_3} - x_{i_2})(y_{i_1} - y_{i_3})}, \quad (19)$$

$$W_{\sigma_0, i_3}(x, y) = 1 - W_{\sigma_0, i_1}(x, y) - W_{\sigma_0, i_2}(x, y). \quad (20)$$

When (x, y) is outside the triangle, all the Whitney 0-forms vanishes. Note that $W_{\sigma_0, i_1}(x, y)$, $W_{\sigma_0, i_2}(x, y)$ and $W_{\sigma_0, i_3}(x, y)$ are the areas of the triangles $\Delta p i_2 i_3$, $\Delta p i_3 i_1$, and $\Delta p i_1 i_2$, respectively. Thus, the weighting of charge deposition with respect to a vertex is the area weighting of the triangle enclosed by the particle and the opposite edge of the vertex. The density plots of $W_{\sigma_0, i_1}(x, y)$, $W_{\sigma_0, i_2}(x, y)$ and $W_{\sigma_0, i_3}(x, y)$ are shown in Fig. 2(a)-(c). Figure 2(a) shows $W_{\sigma_0, i_1}(x, y)$ approaching to 1 as the particle is close to the vertex i_1 . The chosen

Whitney 0-forms in Eqs. (18)-(20) obviously satisfy the condition,

$$\sum_{I=i_1, i_2, i_3} W_{\sigma_0, I}(\mathbf{x}_p) = 1. \quad (21)$$

In the 2D triangular mesh, 1-forms, such as \mathbf{E}_J , are defined on the triangular edges. And the index J for the edges consists of an ordered pair of indices of the vertices. For example, $J = i_1 i_2$ labels the oriented edge from i_1 to i_2 , as shown in Figure 1(b). The discrete gradient operator $\nabla_{dJ, I}$ consistent with Eq. (15) is

$$\nabla_{di_1 i_2, I} = \delta_{i_2 I} - \delta_{i_1 I}. \quad (22)$$

According to the definition of Whitney forms [20], the Whitney 1-form on unstructured triangular mesh is

$$W_{\sigma_1, j' j} = W_{\sigma_0, j} \nabla W_{\sigma_0, j'} - W_{\sigma_0, j'} \nabla W_{\sigma_0, j}. \quad (23)$$

For the triangular mesh, the expressions of $W_{\sigma_1, j' j}(x, y)$ for $j', j = i_1, i_2, i_3$ and $j' \neq j$ are

$$W_{\sigma_1, i_1 i_2}(x, y) = \left[\frac{(y_{i_3} - y_{i_1})W_{\sigma_0, i_1}(x, y) - (y_{i_2} - y_{i_3})W_{\sigma_0, i_2}(x, y)}{(x_{i_1} - x_{i_3})(y_{i_2} - y_{i_3}) + (x_{i_3} - x_{i_2})(y_{i_1} - y_{i_3})}, \right. \\ \left. \frac{(x_{i_1} - x_{i_3})W_{\sigma_0, i_1}(x, y) - (x_{i_3} - x_{i_2})W_{\sigma_0, i_2}(x, y)}{(x_{i_1} - x_{i_3})(y_{i_2} - y_{i_3}) + (x_{i_3} - x_{i_2})(y_{i_1} - y_{i_3})} \right], \quad (24)$$

$$W_{\sigma_1, i_2 i_3}(x, y) = \left[\frac{(y_{i_1} - y_{i_2})W_{\sigma_0, i_2}(x, y) - (y_{i_3} - y_{i_1})W_{\sigma_0, i_3}(x, y)}{(x_{i_1} - x_{i_3})(y_{i_2} - y_{i_3}) + (x_{i_3} - x_{i_2})(y_{i_1} - y_{i_3})}, \right. \\ \left. \frac{(x_{i_2} - x_{i_1})W_{\sigma_0, i_2}(x, y) - (x_{i_1} - x_{i_3})W_{\sigma_0, i_3}(x, y)}{(x_{i_1} - x_{i_3})(y_{i_2} - y_{i_3}) + (x_{i_3} - x_{i_2})(y_{i_1} - y_{i_3})} \right], \quad (25)$$

$$W_{\sigma_1, i_3 i_1}(x, y) = \left[\frac{(y_{i_2} - y_{i_3})W_{\sigma_0, i_3}(x, y) - (y_{i_1} - y_{i_2})W_{\sigma_0, i_1}(x, y)}{(x_{i_1} - x_{i_3})(y_{i_2} - y_{i_3}) + (x_{i_3} - x_{i_2})(y_{i_1} - y_{i_3})}, \right. \\ \left. \frac{(x_{i_3} - x_{i_2})W_{\sigma_0, i_3}(x, y) - (x_{i_2} - x_{i_1})W_{\sigma_0, i_1}(x, y)}{(x_{i_1} - x_{i_3})(y_{i_2} - y_{i_3}) + (x_{i_3} - x_{i_2})(y_{i_1} - y_{i_3})} \right], \quad (26)$$

for (x, y) inside the triangle. All $W_{\sigma_1, j' j}(x, y)$ vanishes when (x, y) is outside the triangle. The amplitude density plot and the quiver plot of $W_{\sigma_1, i_2 i_3}(x, y)$ are showed in Fig. 2(d), where the amplitude approaches zero when a particle is close to the opposite vertex of the edge and maximizes when the particle approaches the edge. Figures 2(e) and (f) plot the value and direction of $W_{\sigma_1, i_3 i_1}(x, y)$ and $W_{\sigma_1, i_1 i_2}(x, y)$.

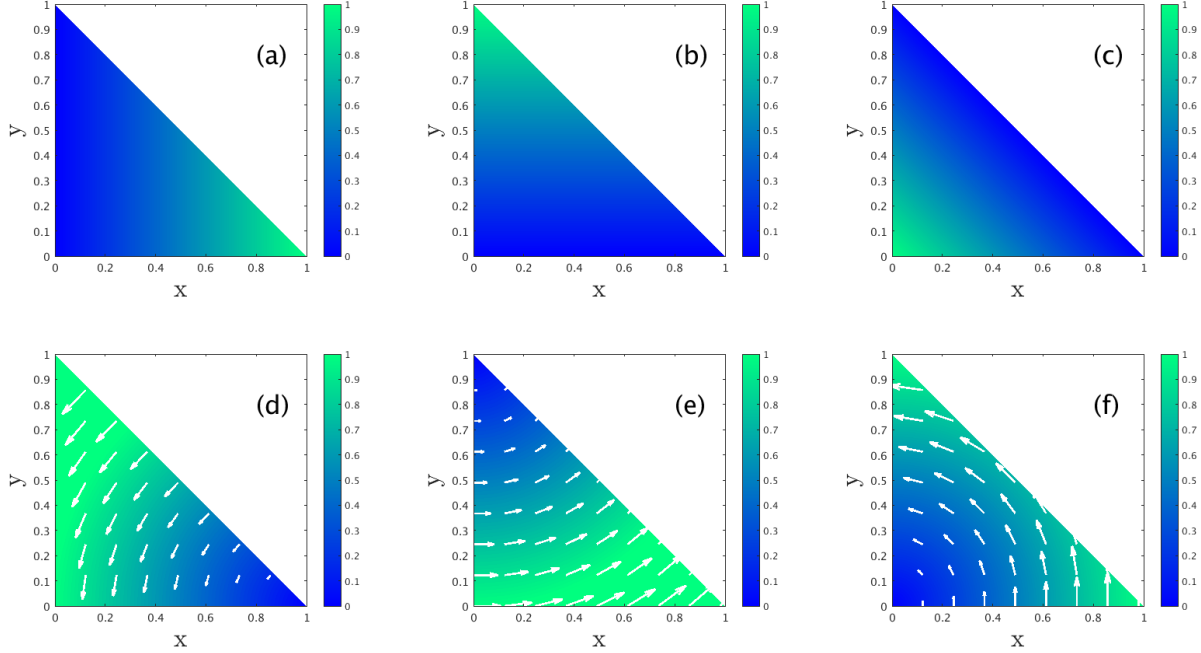


Figure 2. The values of the Whitney 0-forms and 1-forms. The density plot of the value of (a) $W_{\sigma_0, i_1}(x, y)$, (b) $W_{\sigma_0, i_2}(x, y)$, and (c) $W_{\sigma_0, i_3}(x, y)$. The amplitude density plot and the quiver plot of (d) $W_{\sigma_1, i_2 i_3}(x, y)$, (e) $W_{\sigma_1, i_3 i_1}(x, y)$, and (f) $W_{\sigma_1, i_1 i_2}(x, y)$.

After $W_{\sigma_0, I}$, $W_{\sigma_1, J}$ and $\nabla_{dJ, I}$ are chosen, the discrete electric potential ϕ_I at each vertex can be calculated by Eqs. (13) and (12), and the electric field on the edges according to Eq. (17) is

$$E_{i_1 i_2} = \phi_{i_2} - \phi_{i_1}, \quad (27)$$

where $E_{i_1 i_2}$ is a discrete 1-form, we denote it by a boldface symbol in Fig. 1 to following the convention of physicists. Particles' positions and velocities are advanced according to Eq. (16), which interpolates the electrical field at \mathbf{x}_p as $\mathbf{E}(\mathbf{x}_p) = \sum_J W_{\sigma_1, J}(\mathbf{x}_p) E_J$ using Whitney 1-forms. Note that by definition $W_{\sigma_1, J}(\mathbf{x}_p)$ is a vector and E_J is a scalar. This process is illustrated in Fig. 1(c). In the current implementation, Eq. (16) is integrated by the Boris algorithm [43], which preserves the phase space volume [44–48, 55] although is not symplectic.

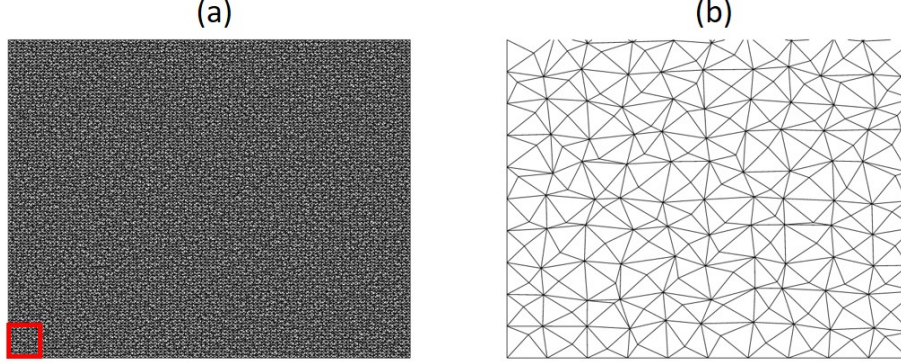


Figure 3. (a) The rectangular simulation domain. (b) The zoom-in of the red rectangular region in (a).

III. ION BERNSTEIN WAVES ON 2D UNSTRUCTURED MESHES

The PIC method described in Sec.II is used to examine Ion Bernstein wave (IBW) [56] in 2D uniform plasmas. The simulations are carried out in a rectangular region with periodic boundary conditions and in a 2D circular region with fixed boundary conditions.

A. IBW with periodic boundary conditions in a rectangular region

First, the IBW in a rectangular region of an uniform plasma is examined on an unstructured mesh with periodic boundary conditions. The simulation domain is shown in Fig. 3(a), and Fig. 3(b) is the zoom-in of the red region in Fig. 3(a). The simulation domain has 20201 vertices and 40000 triangles. To implement the periodic boundary conditions, each vertex at the left boundary is identified with the corresponding vertex at the right boundary. Similar identification is imposed for the top and bottom boundaries. The ion mass is $m_i=1.67\times 10^{-27}\text{kg}$ and charge is $q_i=1.6\times 10^{-19}\text{C}$, the initial ion density is $n_{i0}=10^{20}/\text{m}^3$, the electron and ion temperatures are 1000eV, and the out-of-plane background magnetic field is $B_0=2\text{T}$. The simulation timestep is $\Delta t=0.01/\Omega_i$, and the total number of simulation particles is 5.12×10^7 .

During the simulation, the electric potential ϕ on each vertex is recorded. To analyze the data using the Fast-Fourier Transform (FFT), the ϕ on a rectangular mesh is interpolated from the its values on the vertices of the unstructured mesh. The dispersion relations of

the IBW can be inferred from $\tilde{\phi}(k_x, k_y, \omega)$, where k_x and k_y are the wave numbers in the x - and y -directions, and ω is the angular frequency. Figure 4 plots the contours of the spectral power of $\tilde{\phi}$, and the contour peaks show the dispersion relation k_x - ω at a fixed k_y , where k_x and k_y are normalized to the ion gyroradius ρ_i , and ω to the ion gyrofrequency Ω_i . The contour plots of $\tilde{\phi}$ at $k_y\rho_i=0, 1.0, 2.0, 3.0$ are shown in Figs.4(a)-(d), respectively. The contour plots are compared with the theoretical dispersion relation with kinetic ions and adiabatic electrons [49],

$$1 + \theta \sum_{n=-\infty}^{\infty} \frac{n\Omega_i \Gamma_n(b)}{\omega + n\Omega_i} = 0. \quad (28)$$

Here, $\theta = q_i T_e / q_e T_i$, $b \equiv (k_{\perp} \rho_i)^2$, $\Gamma_n \equiv I_n(b) e^{-b}$, k_{\perp} is the perpendicular wave number, and I_n is n -th modified Bessel function of the first kind. For the present 2D simulation, $k_{\perp} = \sqrt{k_x^2 + k_y^2}$. The dispersion relation in terms of (k_x, k_y, ω) can be directly compared with the dispersion relation from the PIC simulation. The red-dashed lines in Fig.4 are the dispersion relation curves at $k_y\rho_i=0, 1.0, 2.0, 3.0$ from Eq. (28). The dispersion relation from the PIC simulations agree well with the theory.

B. IBW in a 2D circular region with fixed boundary conditions

In this section, we simulate the IBW in a 2D circular domain using an unstructured mesh. The simulation domain is shown in Fig.5(a), and Fig.5(b) is the zoom-in of the red rectangular region in Fig.5(a). The simulation domain has 7477 vertices and 14646 triangles. The physical parameters are the same as in Sec.III A. The total number of simulation particles is 4.9×10^{10} in order to reduce noise and obtain eigenmode structures, and the timestep is $\Delta t = 0.02 / \Omega_i$. The boundary condition is that $\phi=0$ at the most-outside vertices, and particles are reflected when entering the most-outside triangles.

For the FFT analysis, ϕ is interpolated to a diagnostic circular mesh which has 101 co-concentric circles with equal intervals, and 61 grid points are distributed on each circle with the same angular interval. On the diagnostic mesh, ϕ is a function of time t and the radial coordinates (r, θ) . Performing the FFT analysis of $\phi(r, \theta, t)$ along the θ - and t -directions, we discover that for each azimuthal mode number m , the spectrum of the system has a rich structure that can be labeled by two integer indices, n and l . In the neighborhood of each integer harmonics of Ω_i labeled by n , there exists a family of eigenmodes labeled by l . The value of l indicates number of oscillations of the eigenmode in the radial direction. Thus,

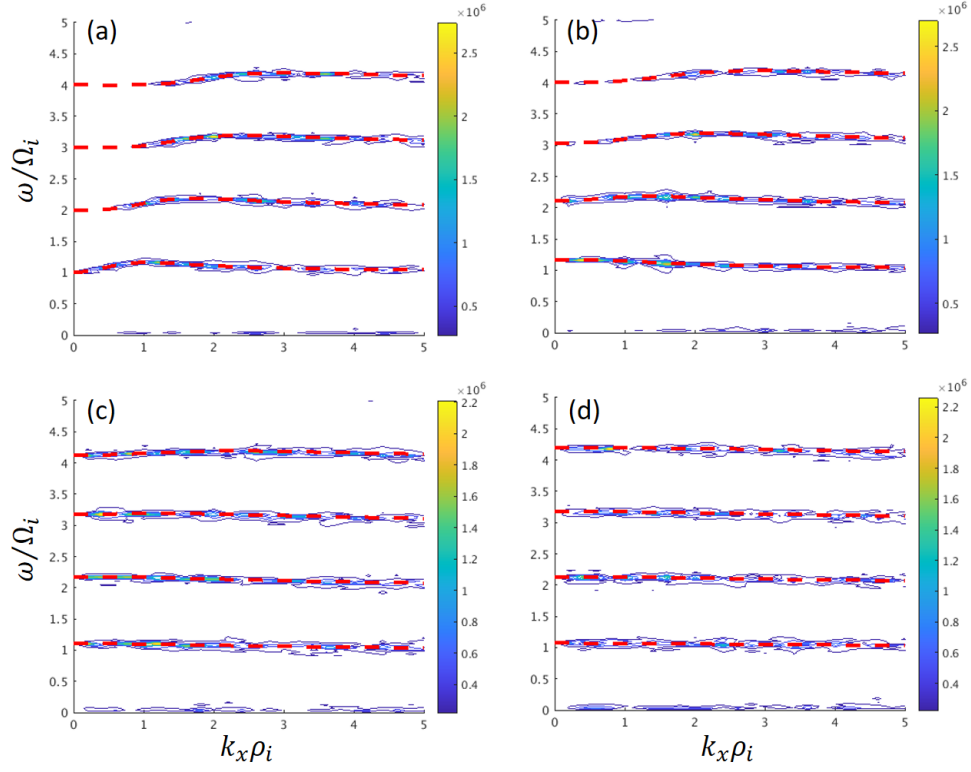


Figure 4. Dispersion relation of the IBW in a 2D rectangular domain. The contour plot of $\tilde{\phi}(k_x, \omega)$ at (a) $k_y \rho_i=0$, (b) $k_y \rho_i=1.0$, (c) $k_y \rho_i=2.0$, and (d) $k_y \rho_i=3.0$. The red dashed lines are the theoretical dispersion relation.

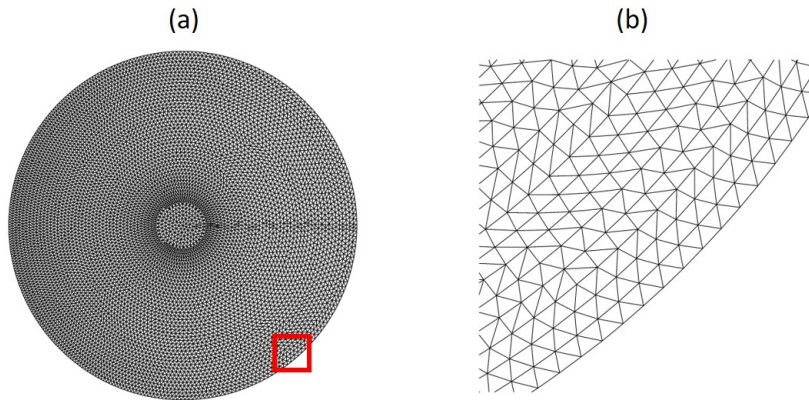


Figure 5. (a) The 2D circular simulation domain. (b) The zoom-in of the red rectangular region in (a).

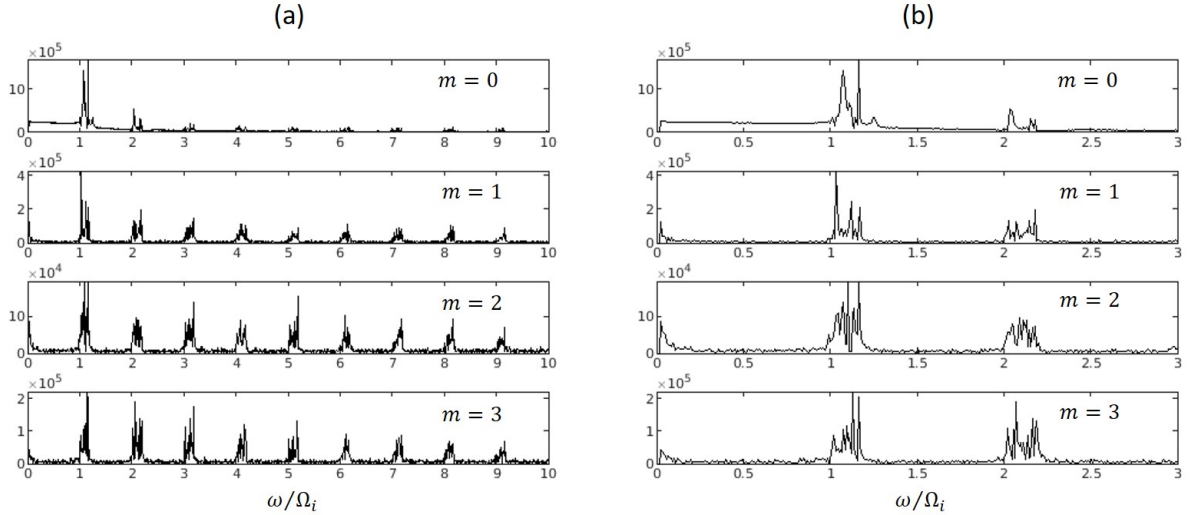


Figure 6. (a) Spectrum of the IBW for $m = 0, 1, 2, 3$. (b) Zoom-in of (a) in $0 \leq \omega/\Omega_i \leq 3$.

the eigenmode expansion for ϕ is

$$\phi = \sum_{n,m,l} \tilde{\phi}_{nml}(r) \exp(im\theta - i\omega_{nml}t), \quad (29)$$

where $\tilde{\phi}_{nml}(r)$ is the eigenfunction of the mode at $\omega = \omega_{nml}$. Figure 6(a) plots the spectrum of $\tilde{\phi}$ for $m = 0, 1, 2, 3$, where the frequency ω is normalized to ion gyro-frequency Ω_i . Figure 6(b) is zoom-in of the spectrum in the range of $0 \leq \omega/\Omega_i \leq 3$. The eigenmode structures $\tilde{\phi}_{nml}(r)$ for $m = 0, 1, 2, 3$, $l = 1, 2, 3$ in the neighborhood of the first harmonic ($n = 1$) are shown in Fig. 7. We are not aware of any previous study of these eigenmodes of the IBW in a circular domain.

IV. COMPARISON OF PIC METHODS ON UNSTRUCTURED MESHES

As discussed in Sec. I, previous PIC methods on unstructured meshes used identical shape function for both charge deposition and field interpolation[6, 7]. In this section, the energy conservation property of our PIC method (Method A) is compared with that of a PIC method (Method B) using identical shape function for both charge deposition and field interpolation. The comparison is carried out on an unstructured mesh as in Fig. 3.

Method B on the unstructured mesh is illustrated in Fig. 8. Suppose a particle at (x, y)

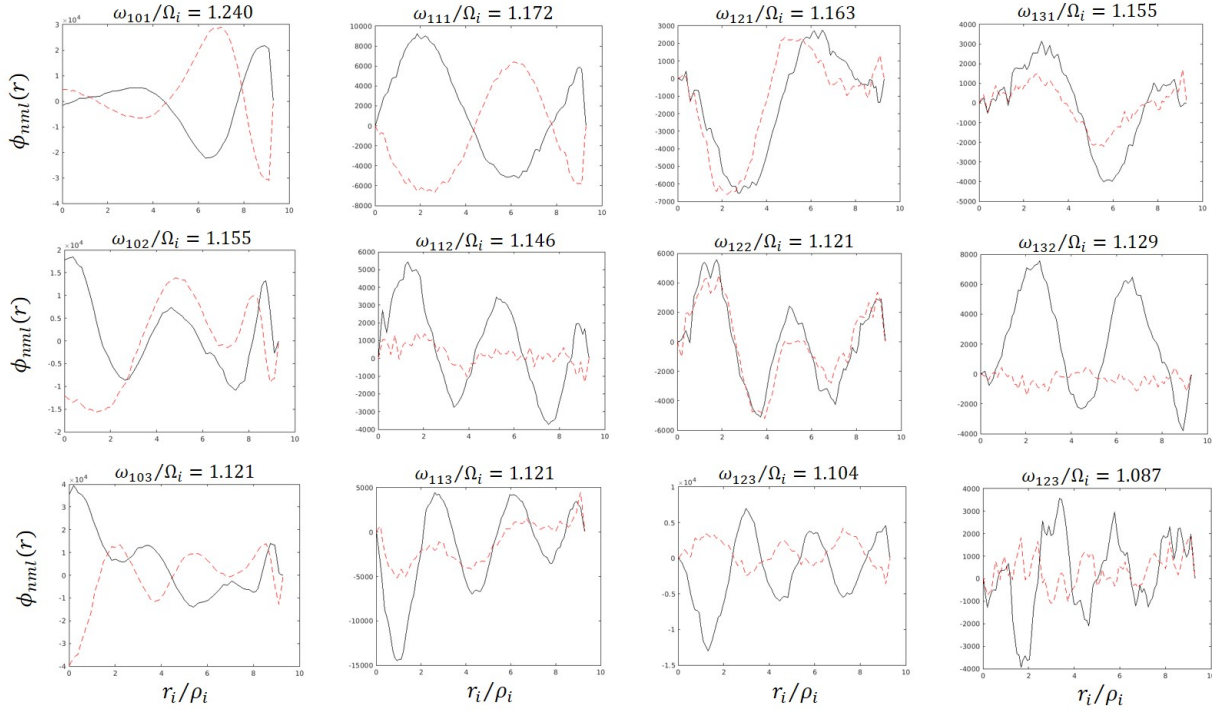


Figure 7. Eigenmode structures $\tilde{\phi}_{nml}(r)$ for $m = 0, 1, 2, 3$ and $l = 1, 2, 3$ in the neighborhood of the first harmonic ($n = 1$). Black solid line is real part of $\tilde{\phi}_{nml}(r)$, and red dashed line is imaginary part. The eigen frequency ω_{nml} for each eigenmode is listed.

is inside a triangle. The charge of the particle is deposited to the triangular vertices by the linear barycentric functions, as shown in Fig. 8(a). The electric potential ϕ_I is calculated from ρ_I by Eq. (12). With the ϕ_I on each vertex, the electric field E_x and E_y are calculated by a centered finite difference method [5]. At (x_{i_1}, y_{i_1}) , the x -component of the electric field is

$$E_x = \frac{\phi(x_{i_1} + \Delta x, y_{i_1}) - \phi(x_{i_1} - \Delta x, y_{i_1})}{2\Delta x}, \quad (30)$$

where $\Delta x, \Delta y$ is chosen to be a small value comparing to the averaged length of triangular edges. To calculate $\phi(x_{i_1} \pm \Delta x, y_{i_1})$, we first determine the triangle in which the point $(x_{i_1} \pm \Delta x, y_{i_1})$ locates, and then interpolating ϕ at $(x_{i_1} \pm \Delta x, y_{i_1})$ from its values on the triangular vertices using linear barycentric functions, as shown in Fig. 8(b). E_y can be calculated using a similar method. As Fig. 8(c) shows, to advance the particle's position and velocity, the \mathbf{E} at the particle's position (x, y) is obtained by interpolating the \mathbf{E} at the

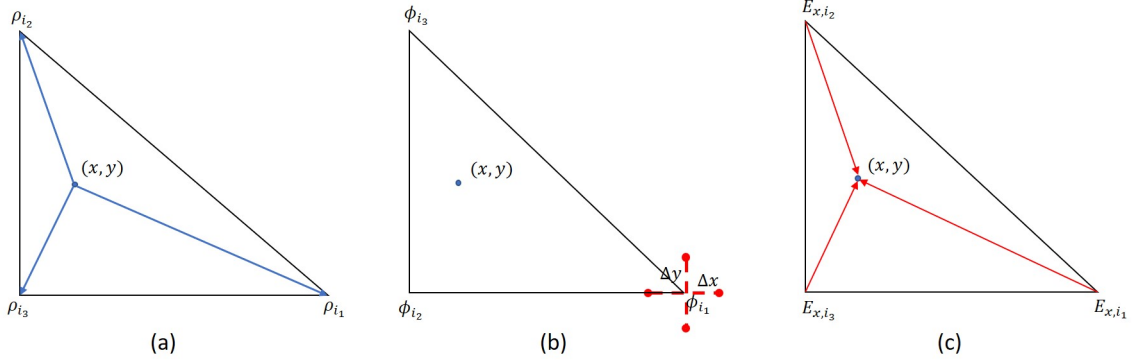


Figure 8. A previous PIC method (Method B) on unstructured meshes with identical shape function for charge deposition and field interpolation. (a) Depositing the particle’s charge into the triangular vertices. (b) Computing E_x and E_y by a five-point finite difference method. (c) Interpolating \mathbf{E} from vertices to the particle’s position.

triangular vertices to (x, y) using the linear barycentric function. Note that the Method B uses the linear barycentric functions for both charge deposition and field interpolation.

Contrast simulations of Methods A and B are carried out on the unstructured mesh with the periodic boundary conditions. The horizontal length of the mesh is 10 times larger than the vertical length. The mesh has 2111 vertices and 4000 triangles. For Method B, Δx is chosen to be 1/10 of averaged length of triangular edges. The physical parameters are the same as in Sec. III A. For both simulations, the timestep is $\Delta t = 0.02/\Omega_i$ and the number of simulation particles is 1.28×10^6 . Both simulations are performed to the time length of $2400/\Omega_i$.

Figure 9(a) shows the comparison of the energy conservation property of Methods A and B. The energy of the system consists of the kinetic energy of particles and the potential energy of the field. We measure the error of total energy during the simulations. The total energy includes plasma kinetic energy, particles’ potential energy and electric field energy. The blue line is the total energy error of Method A, and the red line is that of Method B. The growth rate of total energy error of Method B is 6 times faster than that of Method A. The IBW dispersion relation for $k_y = 0$ at $t \sim 1800/\Omega_i$ is shown in Figures 9(b) and 9(c) for Method A and Method B, respectively. The dispersion relation from Method A agrees well with the theoretical results. In contrast, the contour plot from Method B cannot recover the dispersion relation for all harmonics in the regime of $k_x \rho_i \geq 3$. Method

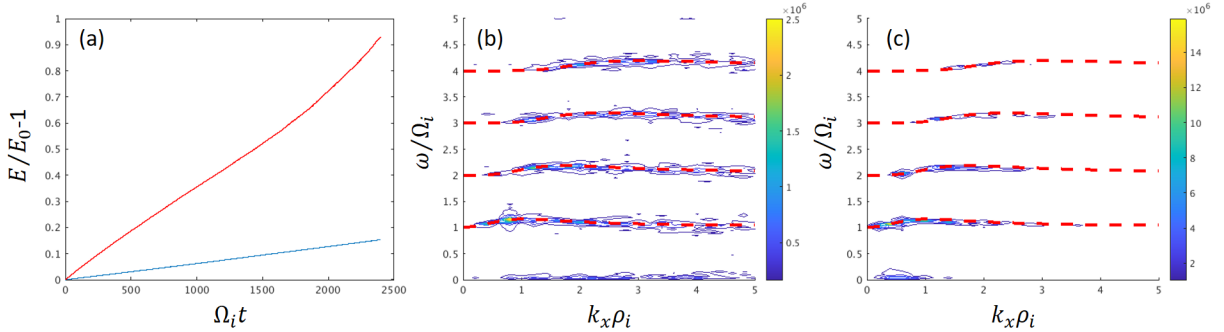


Figure 9. Comparison between our algorithm derived from the discrete variational principle (Method A) and a previous method using identical shape function for charge deposition and field interpolation (Method B). (a) The total energy error during the simulation. The blue curve is for method A and the red curve is for Method B. (b) The dispersion relation obtained from Method A, and the red dashed lines are the theoretical results. (c) The dispersion relation obtained from Method B.

A has a much smaller total energy error, and thus generates a more accurate dispersion relation. This comparison study demonstrates that our new algorithm derived from the discrete variational principle has a much better energy conservation property than previous methods using identical shape function for charge deposition and field interpolation. We want to point out that, many PIC methods adopt identical shape function for both charge deposition and field interpolation in order to conserve momentum. These PIC methods are commonly referred as “momentum conserving” method. However, as Refs. [3, 5] stated, besides using identical shape function for both charge deposition and field interpolation, a PIC method must have “correctly space-centered difference approximation to derivatives” [3] or “left-right symmetry” [5] to have momentum conservation. Solely adopting identical shape function for both charge deposition and field interpolation, as in method B and the previous PIC methods [6–10], can not guarantee momentum conservation on a unstructured mesh.

V. CONCLUSIONS AND DISCUSSION

In conclusion, we have extended the geometric electrostatic PIC method in Ref. [29] to unstructured meshes in 2D simulation domains. The PIC method uses kinetic ions and adi-

abatic electrons. The discrete variational principle gives an algorithm that deposits particle charge to triangular vertices by Whitney 0-forms and interpolates the electric field at particles' positions using its values on the triangular edges and Whitney 1-forms. The formula of Whitney-forms, the DEC method that computes the discrete electric field on triangular edges, and the algorithm of charge-deposition and field-interpolation are described in details. The PIC method has been used to investigate IBWs on unstructured meshes with two different geometries and boundary conditions. For the case with periodic boundary conditions in a rectangular domain, the simulated dispersion relation agrees well with the theory. For the case on a 2D circular unstructured mesh with fixed boundary conditions, the spectrum and eigenmode structures are obtained. The simulation results of our PIC algorithm are compared with those of a previous PIC method using identical shape function for charge-deposition and field-interpolation. The comparison shows the new algorithm has a much better energy conservation property and thus can give a more accurate dispersion relation. The present paper focuses on demonstrating the new charge-deposition and field-interpolation methods on unstructured meshes and has not implemented the symplectic structure-preserving integration algorithm. The topic of symplectic structure-preserving integration on unstructured meshes will be addressed in future studies.

ACKNOWLEDGMENTS

This research was supported by the U.S. Department of Energy Office of Science ASCR and FES through SciDAC-4 Partnership Center for High-fidelity Boundary Plasma Simulation (HBPS), under the contract number DE-AC02-09CH11466 through Princeton University. The computing resources were provided on the PPPL computer Traverse operated by the Princeton Institute for Computational Science and Engineering (PICSciE) and on the leadership class computer Cori at NERSC. The data that support the findings of this study are available from the corresponding author upon reasonable request.

-
- [1] J. M. Dawson, H. Okuda, and B. Rosen, in *Methods in Computational Physics: Advances in Research and Applications* (Elsevier, 1976) pp. 281–325.
 - [2] J. M. Dawson, *Reviews of Modern Physics* **55**, 403 (1983).

- [3] R. Hockney and J. W. Eastwood, *Computer simulation using particles* (McGraw-Hill International Book Co, New York, 1981).
- [4] D. Potter, *Computational Physics* (John Wiley, 1973).
- [5] C. Birdsall and A. B. Langdon, *Plasma physics via computer simulation* (Adam Hilger, Bristol, Eng, 1991).
- [6] M. Celik, M. Santi, S. Cheng, M. Martínez-Sánchez, and J. Peraire, in *28th International Electric Propulsion. Conference, Toulouse, March 2003* (2003).
- [7] A. Spirkin and N. A. Gatsonis, *Computer Physics Communications* **164**, 383 (2004).
- [8] N. A. Gatsonis and A. Spirkin, *Journal of Computational Physics* **228**, 3742 (2009).
- [9] D. M. Day, *Numerical Experiments on Unstructured PIC Stability*, Tech. Rep. (Sandia National Laboratories, 2011).
- [10] D. Han, P. Wang, X. He, T. Lin, and J. Wang, *Journal of Computational Physics* **321**, 965 (2016).
- [11] A. Langdon, *Journal of Computational Physics* **6**, 247 (1970).
- [12] J. Squire, H. Qin, and W. M. Tang, *Physics of Plasmas* **19**, 084501 (2012).
- [13] J. Squire, H. Qin, and W. M. Tang, *Geometric Integration of the Vlasov-Maxwell System with a Variational Particle-in-cell Scheme*, Tech. Rep. PPPL-4748 (Princeton Plasma Physics Laboratory, 2012).
- [14] T. Lee, *Physics Letters B* **122**, 217 (1983).
- [15] A. P. Veselov, *Functional Analysis and Its Applications* **22**, 83 (1988).
- [16] J. E. Marsden and M. West, *Acta Numerica* **10**, 357 (2001).
- [17] H. Qin and X. Guan, *Physical Review Letters* **100**, 035006 (2008).
- [18] H. Qin, X. Guan, and W. M. Tang, *Physics of Plasmas* **16**, 042510 (2009).
- [19] H. Qin, *Scientific Reports* **10**, 19329 (2020).
- [20] H. Whitney, *Geometric integration theory* (Princeton University Press, 1957).
- [21] A. Bossavit, *Computational electromagnetism: variational formulations, complementarity, edge elements* (Academic Press, San Diego, 1998).
- [22] A. N. Hirani, *Discrete exterior calculus*, Ph.D. thesis, California Institute of Technology (2003).
- [23] J. Xiao, H. Qin, J. Liu, Y. He, R. Zhang, and Y. Sun, *Physics of Plasmas* **22**, 112504 (2015).
- [24] J. Xiao, H. Qin, and J. Liu, *Plasma Science and Technology* **20**, 110501 (2018).
- [25] A. S. Glasser and H. Qin, *Journal of Plasma Physics* **86**, 835860303 (2020).

- [26] J. Xiao, J. Liu, H. Qin, and Z. Yu, *Physics of Plasmas* **20**, 102517 (2013).
- [27] J. Xiao, J. Liu, H. Qin, Z. Yu, and N. Xiang, *Physics of Plasmas* **22**, 092305 (2015).
- [28] J. Xiao, H. Qin, J. Liu, and R. Zhang, *Physics of Plasmas* **24**, 062112 (2017).
- [29] J. Xiao and H. Qin, *Nuclear Fusion* **59**, 106044 (2019).
- [30] J. Xiao and H. Qin, “Explicit structure-preserving geometric particle-in-cell algorithm in curvilinear orthogonal coordinate systems and its applications to whole-device 6D kinetic simulations of tokamak physics,” (2020), 2004.08150v1 [physics.plasm-ph].
- [31] J. Zheng, J. Chen, F. Lu, J. Xiao, H. An, and L. Shen, *Plasma Physics and Controlled Fusion* **62**, 125020 (2020).
- [32] Y. He, H. Qin, Y. Sun, J. Xiao, R. Zhang, and J. Liu, *Physics of Plasmas* **22**, 124503 (2015).
- [33] H. Qin, J. Liu, J. Xiao, R. Zhang, Y. He, Y. Wang, Y. Sun, J. W. Burby, L. Ellison, and Y. Zhou, *Nuclear Fusion* **56**, 014001 (2016).
- [34] Y. He, Y. Sun, H. Qin, and J. Liu, *Physics of Plasmas* **23**, 092108 (2016).
- [35] M. Kraus, K. Kormann, P. J. Morrison, and E. Sonnendrücker, *Journal of Plasma Physics* **83**, 905830401 (2017).
- [36] J. W. Burby, *Physics of Plasmas* **24**, 032101 (2017).
- [37] P. J. Morrison, *Physics of Plasmas* **24**, 055502 (2017).
- [38] Y. Li, Y. He, Y. Sun, J. Niesen, H. Qin, and J. Liu, *Journal of Computational Physics* **396**, 381 (2019).
- [39] B. Perse, K. Kormann, and E. Sonnendrücker, <http://arxiv.org/abs/2002.09386v1>.
- [40] K. Kormann and E. Sonnendrücker, *Journal of Computational Physics* **425**, 109890 (2021).
- [41] H. Moon, F. L. Teixeira, and Y. A. Omelchenko, *Computer Physics Communications* **194**, 43 (2015).
- [42] Y. He, Z. Zhou, Y. Sun, J. Liu, and H. Qin, *Physics Letters A* **381**, 568 (2017).
- [43] J. Boris, in *Proceedings of the Fourth Conference on Numerical Simulation of Plasmas* (Naval Research Laboratory, Washington D. C., 1970) p. 3.
- [44] H. Qin, S. Zhang, J. Xiao, J. Liu, Y. Sun, and W. M. Tang, *Physics of Plasmas* **20**, 084503 (2013).
- [45] Y. He, Y. Sun, J. Liu, and H. Qin, *Journal of Computational Physics* **281**, 135 (2015).
- [46] R. Zhang, J. Liu, H. Qin, Y. Wang, Y. He, and Y. Sun, *Physics of Plasmas* (1994-present) **22**, 044501 (2015).

- [47] Y. He, Y. Sun, J. Liu, and H. Qin, [Journal of Computational Physics](#) **305**, 172 (2016).
- [48] Y. He, Y. Sun, R. Zhang, Y. Wang, J. Liu, and H. Qin, [Physics of Plasmas](#) **23**, 092109 (2016).
- [49] B. Sturdevant, *Fully Kinetic Ion Models for Magnetized Plasma Simulations*, Ph.D. thesis, University of Colorado (2016).
- [50] B. J. Sturdevant, Y. Chen, and S. E. Parker, [Physics of Plasmas](#) **24**, 081207 (2017).
- [51] W. Horton, [Reviews of Modern Physics](#) **71**, 735 (1999).
- [52] J. Weiland, *Stability and Transport in Magnetic Confinement Systems* (Springer New York, 2012).
- [53] Y. Hu, M. Miecniowski, Y. Chen, and S. Parker, [Plasma](#) **1**, 105 (2018).
- [54] M. T. Miecniowski, B. J. Sturdevant, Y. Chen, and S. E. Parker, [Physics of Plasmas](#) **25**, 055901 (2018).
- [55] C. Ellison, J. Burby, and H. Qin, [Journal of Computational Physics](#) **301**, 489 (2015).
- [56] I. B. Bernstein, [Physical Review](#) **109**, 10 (1958).